POLITECNICO
MILANO 1863

SCUOLA DI INGEGNERIA INDUSTRIALE
E DELL'INFORMAZIONE

Executive Summary of the Thesis

High-precision Mobile Positioning for Automotive SAR Imaging

Laurea Magistrale in Telecommunication Engineering - Ingegneria delle Telecomunicazioni

Author: Pietro Morri

Advisor: Prof. Monica Nicoli

Co-advisor: Giovanni Ciaramitaro

Academic year: 2021-2022

1. Introduction

Synthetic Aperture RADAR (SAR) is a promising imaging technology for the automotive industry [1]. To improve the standard RADAR architecture, they increase the antennas density by synthesizing virtual elements in a time interval along the vehicle's trajectory. To effectively produce sharp images the imaging algorithm requires the knowledge of the RADAR's position and velocity with a high degree of accuracy within a synthetic aperture. The work of this thesis is to implement a precise navigation system to aid the RADAR in focusing the images, based on the architecture described in [2]. The navigation algorithms we developed are based on the Unscented Kalman Filter (UKF), a nonlinear Bayesian estimator. Two variations of the basic algorithm are proposed in order to fuse more information from the motion models: a standard Interacting Multiple Model (IMM) and a threshold-based system. A second analysis was made by using different combinations of correction sensors and their impact was evaluated on the SAR images. The algorithms process real data collected in an experimental campaign. The results are validated by a Real Time Kinematics (RTK) Global Navigation Satellite System (GNSS).

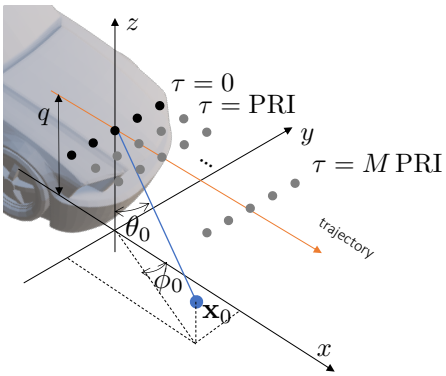

Figure 1: RADAR configuration.

2. SAR Principles

SAR systems exploit the motion of the RADAR to create a virtual array of antennas. The elements of the synthetic array correspond to the position of the antenna in different time instants. We assume that the SAR sends and receives echoes of a single pulse every slow time interval τ, after which it moves once more (the "stop and go assumption").
Let us now consider the 3D scenario of a single antenna SAR mounted on a car moving along

direction x and a target in $\mathbf{x}_0 = [x_0,\ y_0,\ z_0]$ as depicted in fig. 1. Considering a Multiple Input Multiple Output (MIMO) SAR system the MIMO image obtained with the Time Domain Back Projection (TDBP) algorithm is given by equation [2, eq. (11)] In order to improve resolution, a commonly used procedure is the so-called autofocus. Low resolution MIMO images are taken as input and with the aim to compensate for the residual phase error. Once the estimates of the residual velocities have been computed [2], it is possible to find for each slow time τ the estimated of residual phase $\Delta\hat{\psi}(\mathbf{x},\tau) = (\mathbf{k}(\mathbf{x})^T\Delta\hat{\mathbf{v}})\tau$ and compute the N phase compensated low resolution image:

$$\hat{I}_m(\mathbf{x},\tau) = I_m(\mathbf{x},\tau)e^{-j\Delta\hat{\psi}(\mathbf{x},\tau)} \tag{1}$$

where $\mathbf{k}(\mathbf{x}) = \frac{4\pi}{\lambda}[\sin\theta\cos\theta, \sin\theta\sin\theta, \cos\theta]^T$ and $\Delta\hat{\mathbf{v}}$ is the velocity error. By coherently summing them along the synthetic aperture,

$$I(\mathbf{x}) = \sum_{\tau\in T}\hat{I}_m(\mathbf{x},\tau), \tag{2}$$

we get the final SAR image.

3. Tracking Filters

As a navigation algorithm we adopted the Unscented Kalman Filter (UKF). The filter is based on the Unscented Transform, a procedure to calculate the statistics of a random variable which is fed to a non-linear function by using a set of points called *sigma points*. This tool is particularly effective if compared to the EKF, which is another alternative to use when the motion and measurements models are non-linear. Indeed, the UKF uses a deterministic technique that determines points which, once passed through the non-linear system, preserve the statistical description of the a-posteriori probability up to the 2nd order, at the same computational cost of the EKF ($\mathcal{O}(L^3)$ for both cases where L is the dimension of the state) [3].

3.1. Measurement Models

For the observation functions we introduce the measurement models for the on-board sensors equipped in the car. The car is equipped with a GPS that provides the user's position. The measurements are linked to the state variables through the following equations:

$$\mathbf{y}_\mathbf{p}^{GPS}(k) = \mathbf{p}(k) + \mathbf{n}_\mathbf{p}^{GPS}(k), \tag{3}$$
$$y_v^{GPS}(k) = v(k) + n_v^{GPS}(k), \tag{4}$$
$$y_\theta^{GPS}(k) = \theta(k) + n_\theta^{GPS}(k), \tag{5}$$

where the measurement noise is an additive Gaussian random variable, i.e., $\mathbf{n_p} \sim \mathcal{N}(0, \mathbf{\Sigma}_p^{GPS})$, $n_v \sim \mathcal{N}(0, {\sigma_v^{GPS}}^2)$ and $n_\theta \sim \mathcal{N}(0, {\sigma_\theta^{GPS}}^2)$.
The Inertial Measurement Unit (IMU), mounted on the vehicle's centre of gravity, provides inertial navigation data from an accelerometer and a gyroscope. The accelerometer provides the linear acceleration whereas the gyroscope the angular velocity, both in the body frame. IMU's measurements are modelled as:

$$\mathbf{y}_a(k) = \mathbf{a}(k) + \mathbf{b}_\mathbf{a}^{IMU} + \mathbf{n}_\mathbf{a}^{IMU} \tag{6}$$
$$y_\omega(k) = \omega(k) + b_\omega^{IMU} + n_\omega^{IMU} \tag{7}$$

where $\mathbf{n}_\mathbf{a}^{IMU} \sim \mathcal{N}(\mathbf{0}, \mathbf{\Sigma}_\mathbf{a}^{IMU})$ and $\mathbf{n}_\omega^{IMU} \sim \mathcal{N}(0, {\sigma_\omega^{IMU}}^2)$. In equations (6), (7), $\mathbf{b}_\mathbf{a}^{IMU}$ and b_ω^{IMU} are the bias affecting the sensors.
From the car's electronic control unit we take data provided by a Steering Angle Sensor (SAS). The observation equation combines the car speed, yaw rate and the constant term of the wheelbase $L \in \mathbb{R}$ to obtain the wheel's steering angle:

$$y^{SAS} = -\arctan\left(\frac{L\omega(k)}{v}(k)\right) + n^{SAS}(k) \tag{8}$$

In the former equation $n^{SAS}(k) \sim \mathcal{N}(0, {\sigma^{SAS}}^2)$ is the Gaussian measurement noise. The last model we consider embeds the information coming from four Wheel Odometers (WO), one per wheel, once again embedded in the ECU. Its measurement model is:

$$y_v^{WO}(k) = v(k) + n_v^{odometer}(k), \tag{9}$$

with $n_v^{WO}(k) \sim \mathcal{N}(0, {\sigma^{odometer}}^2)$.

3.2. Motion Models

Each model best describes a driving scenario and it is common practice to just use a comprehensive model for a given trajectory. The state is a column $\mathbf{x}_k \in \mathbb{R}^{11}$ composed by the following elements:

$$\mathbf{x}(k) = [\mathbf{p}(k), \mathbf{v}(k), \mathbf{a}(k), \theta(k), \omega(k), b_\mathbf{a}(k), b_\omega(k)]^T. \tag{10}$$

In this work we considered the Constant Velocity (CV), Constant Acceleration (CA), Constant Turn Rate and Velocity (CTRV), Constant Turn Rate and Acceleration (CTRA) models [4].

3.3. Multiple Model Filters

In order to fuse information from all these models, two improvements were considered. The first one is the Interacting Multiple Model (IMM) filter which creates different instances of the models and uses them to perform separate estimates that then get combined as a weighted sum. The second relies on a threshold based switch which chooses at every time sample k the model which best fits the driving scenario according to the sensors measures. Even if the expected performance of the latter approach should be slightly inferior to the IMM, as propagating four models at a time retains more information on the trajectory, this approach should be considered an alternative in the cases where computational cost is an issue.

4. Experimental Results

4.1. Experimental Campaign

Two experimental campaigns were carried out in order to collect data for processing. The experimental vehicle for the tests is an Alfa Romeo Giulia Veloce, from the Move research group of Politecnico di Milano. The car is equipped with: (i) the Scanbrick® RADAR by Aresys® based on the AWR1243 77-GHz FMCW transceiver by Texas Instruments, with 8 channels (2 Tx and 4 Rx antennas) and 1GHz of bandwidth (resulting in a range resolution of 15cm) mounted on the front bumper at about 0.5m from the ground in a forward-looking configuration; (ii) the RTK system illustrated in section, comprising of the INS Piksi board, mounted on the car's Center of Gravity (CoG), the GNSS antenna, attached to the car's roof and the Freewave radio, placed inside the car; (iii) the Inertial Navigation System (INS) xProGPS_nano by Suchy Data Systems, which includes a GNSS receiver, whose antenna is mounted externally on the car's roof, and an IMU, placed in the vehicle's CoG, providing linear acceleration and angular velocity.
Moreover, the employed vehicle is equipped with measurements from several on-board built-in sensors, whose measurements are made available

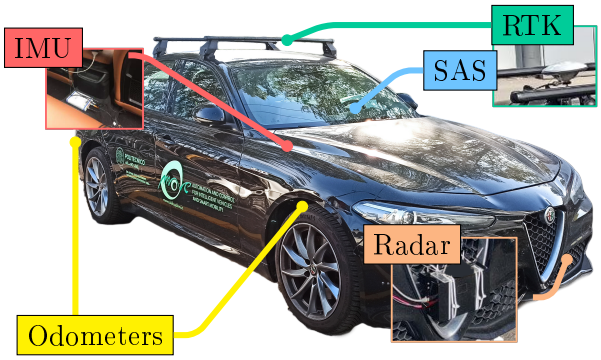

Figure 2: The Alfa Romeo Giulia Veloce experimental car used for the campaign, together with graphical representation of the on-board sensors.

Table 1: On-board sensors parameters

Measurement (sensor)	f_s [Hz]	Measurement error (std)
Position (GNSS)	10	1 [m]
Speed (GNSS)	10	0.1 [m/s]
Heading (GNSS)	10	0.3 [deg]
Yaw rate (IMU)	100	0.1 [rad/s]
Wheel speed (odometer)	50	0.01 [m/s]
Steering angle	50	0.1 [deg]

for research purposes by the car's manufacturer. Among these, we collected the measurements of the SAS, four wheel odometers which will be referred to as INCA measurements. The RTK base was placed in a fixed position in front of the Electronic, Information and Bioengineering Department (DEIB) of Politecnico di Milano at about 15 m of altitude. Figure 2 illustrates the sensors mounted on the vehicle.

4.2. Test 1

This section presents the results obtained by filtering the data acquired during the campaigns detailed with the conventional, the switch-based UKF and a standard UKF employing the CTRV motion model. The accuracy of the three filters is analysed by comparing the outputs to the ground truth data provided by the RTK GNSS. The finite states filter employs the thresholds reported in table 2.The trajectory was collected on the 22/05/2022 at 14:12 PM and lasts 142.4 s. The test was conducted in a densely populated area at a time with a high activity. These condi-

Table 2: Finite states filter thresholds values

Threshold	value	unit
a_{LT}	0.25	[m/s^2]
a_{HT}	0.5	[m/s^2]
ω_{LT}	0.4	[deg/s]
ω_{HT}	0.6	[deg /s]

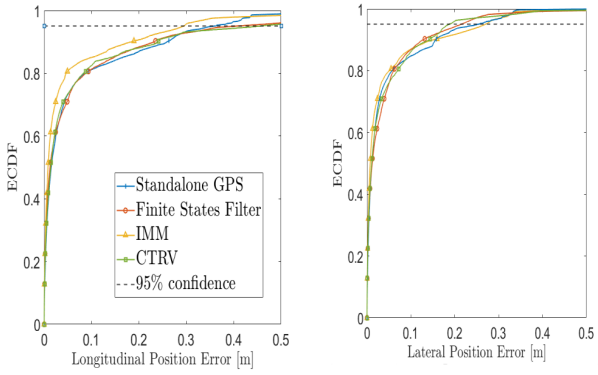

(a) (b)

Figure 3: Relative position error ECDF computed with different motion models.

tions replicate the employment of Sensor-Aided SAR in a urban scenario.
The ECDF of the relative position error relative to a synthetic aperture $A_s = 50$ cm in the two components is reported in figure 3. We can observe that the position errors of the IMM and the finite states filter are very close to the standalone GPS. The improvement is in the order of 5 cm for the longitudinal component of the IMM over the GPS, whereas no significant improvement is noticeable in the lateral position.
Figures 4a and 4b show the ECDF of the relative velocity error in the two longitudinal and lateral components. Again the IMM is the filter giving the best performance. For the longitudinal component the IMM can provide a improvement up to almost 0.05 $\frac{m}{s}$ and the finite states filters is around 0.1 $\frac{m}{s}$. Similar results are obtained for the lateral component. The trend is maintained in the velocity where again the IMM is more accurate. As we can see by comparing the performance of the traditional IMM to the other model switcher, we can see that the IMM deals a better performance in every situation. This result is expected, as the IMM retains more information than the other approach since four different instances of the model are deployed in

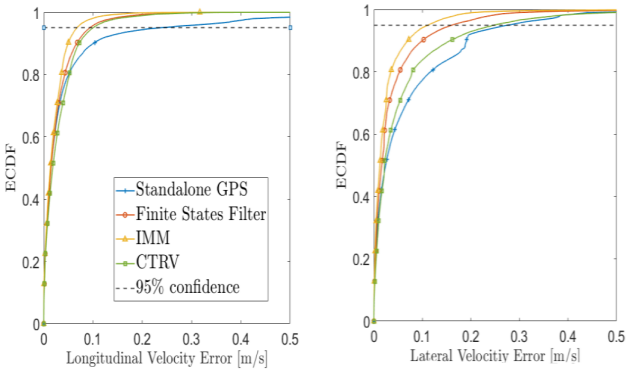

(a) (b)

Figure 4: Relative velocity error ECDF computed with IMM and finite states filter.

Table 3: Different sensors combinations

	Sensors	Observation eq.
Set 1	GNSS, IMU	(3), (4), (5), (6), (7)
Set 2	GNSS, IMU, SAS	(3), (4), (5), (6),(7), (8)
Set 3	GNSS, IMU, ODOM	(3), (4),(5), (6),(7), (9)
Set 4	GNSS, IMU, SAS, ODOM	(3), (4),(5), (6),(7), (8), (9)

parallel and then fused together. This accuracy enhancement, however, causes an increase of the computational complexity.

4.3. Test 2

The results shown in previous section show no significant improvements brought by the IMM and switch-based filter with respect to the CTRV. The latter is hence chosen as motion model for the following analysis, in favour of the computational cost. Then we considered the four sets of table 3 corresponding to probable sensor availability scenarios. This analysis is carried out to search for the minimum number of measurements to enable sensor-assisted SAR. The trajectory consists of a straight motion in front of DEIB and was collected on the 22/05/2022 at 14:09 PM. The measurements last $T = 24.03$ s.
Figure 5 shows the ECDF of the position error in the body frame, along the longitudinal lat-

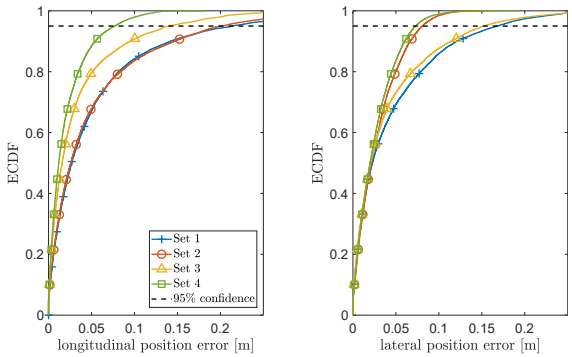

Figure 5: Position Error ECDF

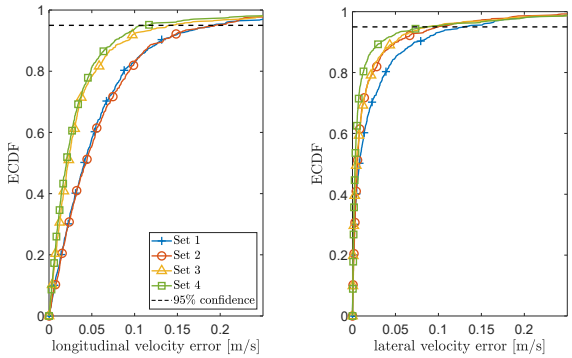

Figure 6: Velocity Error ECDF

itudinal components X^bY^b . In figure 5a the longitudinal component of the error shows two opposite cases, i.e., Profile 1 and 4, which are the sets with the least (GPS, IMU) and most (GPS, IMU, SAS, WO) sensor corrections respectively. The position error in a synthetic aperture for profile 4 goes down to less than 10 cm in 95 % of the cases, more than half the position error of profile 1 which is around 20 cm. Similarly we can say for the lateral component in figure 5b where the amount of sensors used for corrections is related to an improvement in accuracy. We notice how introducing the SAS brings a negligible improvement to the longitudinal components of both position whereas it is useful to estimate the lateral drifts in position. The WO instead proves to be a very important sensor to improve the position errors, in an opposite behaviour with respect to the SAS. The longitudinal position error is more than halved in set 4 with respect to the first two sets, with 95 % of the values in within 10 cm. In the lateral case also set 2 gives the same performance of the position error by reducing it from 15 cm of profile 1 and 3 to almost 5 cm.

Finally, SAR images are focused over a synthetic aperture of 50 cm. In figure 7 are reported the final images in longitudinal-lateral coordinates, i.e. the X^bY^b plane of the body frame.

As we can see comparing the pictures, there are not many significant differences. The most noticeable difference is highlighted in the green box, i.e., a car parked in the side spots. We can see that the images are consistent with the navigation accuracy with the sets 3 and 4 delivering slightly sharper images. The low impact of changing sensors on the final images is due to the autofocus procedure employed to obtain the images. The latter corrects the velocity estimation provided by the navigation to reach mm-level accuracy. The autofocus procedure in fact uses the navigation estimated velocity as an a-priori information which gets refined by the WLS estimate of the residual phase. For this reason, due to the increase in computational complexity (though marginal with respect to the SAR image processor) and economical cost brought by the introduction of the WO and SAS sensors it might not be worth to adopt them to improve the image resolution. It is worth remarking that these tests were performed at moderate speed, in straight trajectories and in good satellite visibility. In a realistic scenario the trajectories are more complex and often galleries and urban canyons degrade the GNSS position. In these scenarios, the SAS and WO could compensate the loss of the GNSS signal as a correction source for the navigation algorithm. Furthermore, in this analysis no turns were considered. This introduces various problems in the image focusing procedures commonly employed. For this reason we expect that the SAS could introduce valuable correcting information bringing the robustness needed to achieve a sufficient resolution.

5. Conclusions

To enhance the filters performance, the calibration should be done on a much larger and diverse set of trajectories. This applies both to measuring the sensors bias and to finding the threshold values for the finite states filter. Future developments of this work will consider new experimental campaigns with more complex trajectories and landscapes. In particular it is worth in-

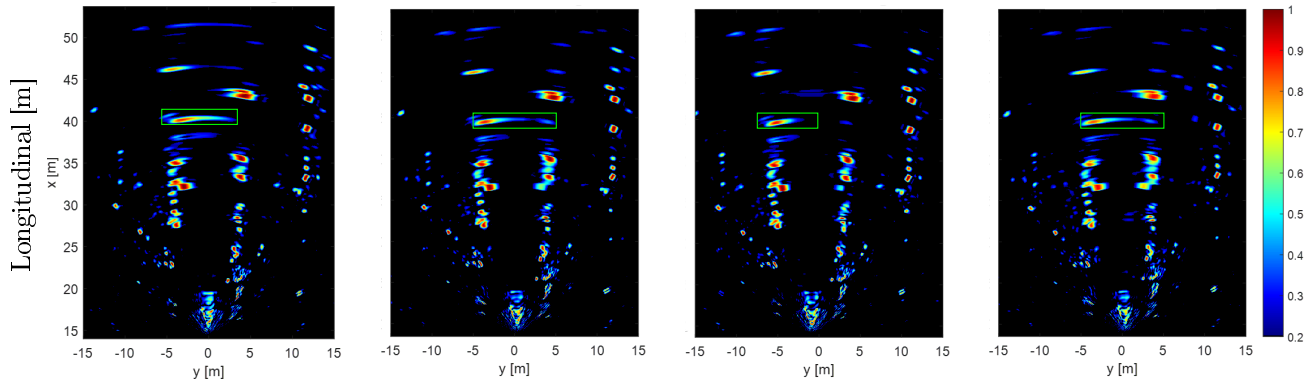

(a) (b) (c) (d)

Figure 7: Velocity Error ECDF

vestigating the performance in curve trajectories where the enhancement of navigation accuracy brought by the SAS is expected to be more evident. Moreover it would be useful to develop the navigation algorithm without providing the GNSS corrections. This is because the GNSS is the most likely sensor to fail in providing corrections whereas the others are always available on the vehicle.

References

[1] Christian Waldschmidt, Juergen Hasch, and Wolfgang Menzel. Automotive radar — from first efforts to future systems. *IEEE Journal of Microwaves*, 1(1):135–148, 2021.

[2] Marco Manzoni, Dario Tagliaferri, Marco Rizzi, Stefano Tebaldini, Andrea Virgilio Monti Guarnieri, Claudio Maria Prati, Monica Nicoli, Ivan Russo, Sergi Duque, Christian Mazzucco, and Umberto Spagnolini. Motion Estimation and Compensation in Automotive MIMO SAR. *IEEE Transactions on Intelligent Transportation Systems*, pages 1–17, Nov. 2022.

[3] Eric A. Wan and Rudolph van der Merwe. *The Unscented Kalman Filter*, chapter 7, pages 221–280. John Wiley and Sons, Ltd, 2001.

[4] Robin Schubert, Eric Richter, and Gerd Wanielik. Comparison and evaluation of advanced motion models for vehicle tracking. In *2008 11th International Conference on Information Fusion*, pages 1–6, 2008.